

East-west asymmetry in the distribution of rainfall in the Chinese Loess Plateau during the Holocene

Duo Wu^{a,*}, Chenbin Zhang^b, Tao Wang^a, Li Liu^a, Xiaojian Zhang^c, Zijie Yuan^a, Shengli Yang^a, Fahu Chen^{a,b}

^a College of Earth and Environmental Sciences, MOE Key Laboratory of Western China's Environmental Systems, Lanzhou University, Lanzhou 730000, China

^b Institute of Tibetan Plateau Research, Key Laboratory of Alpine Ecology, Chinese Academy of Sciences, Beijing 100101, China

^c School of Geography and Ocean Science, Nanjing University, Nanjing 210023, China

ARTICLE INFO

Keywords:

Loess-paleosol sequence
Chinese Loess Plateau
Holocene precipitation
East Asian summer monsoon
East-west asymmetry
Western Pacific subtropical high

ABSTRACT

As the cradle of Chinese civilization the Chinese Loess Plateau (CLP) and its climatic and environmental history have attracted much research attention; however, the spatial characteristics of Holocene climatic conditions across the CLP remains unclear. We investigated five loess sections from the Ganjia Basin in the western CLP, and used paleoclimatic indexes from one well-dated loess-paleosol sequence to reconstruct precipitation variation during the past ~15,000 years. The chronology of the loess section is well established, based on 12 AMS ¹⁴C dates from bulk organic matter. Loess deposited before 8 ka (1 ka = 1000 years before 1950 CE) indicates that precipitation was low from ~15 to 8 ka. Subsequently, a paleosol, characterized by higher magnetic susceptibility and more negative organic carbon isotopic values, developed under the moist conditions of the middle to late Holocene. Comparison with paleoclimatic records from the CLP revealed that precipitation across the CLP was low during the early Holocene and reached its highest level during 8–3 ka, against the background of an enhanced East Asian summer monsoon (EASM). In the eastern CLP (the region east of the Liupan Mountains), the climate became dry after 3 ka because of a weakening of the EASM; however, precipitation in the western CLP was relatively high at this time. This observation of an east–west asymmetry in precipitation in the CLP during the Holocene based on geological data is supported by numerical modeling results from PMIP3, which indicate that it could have been caused by the westward extension of the western Pacific subtropical high. Our findings provide an analog for the study of interglacials on a longer time-scale and they demonstrate that the pattern of moisture conditions between the eastern and western CLP may differ on sub-orbital timescales.

1. Introduction

The Chinese Loess Plateau (CLP) is the cradle of ancient civilization in China. The climate and environment of the region, which is situated in central China, is significantly influenced by the East Asian summer monsoon (EASM), and the extensive loess deposits are valuable archives of monsoon precipitation variations on various timescales. It is widely accepted that a strengthened EASM brings more rainfall to the region and results in stronger pedogenesis; whereas a weakened EASM results in less rainfall and reduced loess weathering intensity (An et al., 1991; Lu et al., 2013; Maher, 2016). Because rain-fed agriculture is highly dependent on precipitation, variations in monsoon intensity and hence precipitation affect the livelihood of millions of people in this densely populated region. A favorable natural environment, with wet and warm

climatic conditions, is critical for societal development and human welfare.

Earlier paleoclimatic studies of the CLP have identified a ‘warm and/or wet’ Holocene climatic optimum (HCO), and Shi et al. (1994), for example, reported a Holocene ‘megathermal’ between 8.5 ka and 3 ka. However, An et al. (2000) proposed the possible asynchronous timing of the HCO, as defined by peak in EASM precipitation across China; and proposed that the precipitation maximum occurred during the interval from 10 ka to 7 ka in north-central and northern east-central China, covering the whole of the CLP (An et al., 2000). In recent years, several well-dated pollen-based precipitation reconstructions have been obtained from the sediments of lakes in northern China. They reveal a gradually intensifying monsoon during the early Holocene, with maximum monsoon intensity during the middle Holocene, and a rapidly

* Corresponding author.

E-mail address: dwu@lzu.edu.cn (D. Wu).

<https://doi.org/10.1016/j.catena.2021.105626>

Received 27 February 2021; Received in revised form 14 July 2021; Accepted 24 July 2021

Available online 31 July 2021

0341-8162/© 2021 The Author(s).

Published by Elsevier B.V. This is an open access article under the CC BY-NC-ND license

(<http://creativecommons.org/licenses/by-nc-nd/4.0/>).

weakening monsoon during the late Holocene (Chen et al., 2015a). This middle Holocene precipitation maximum is also documented by soil development in the loess deposits in the CLP, and in the northern sandy lands of China (Lu et al., 2013; Wang et al., 2014).

Based on the proposal that precipitation amount in northern China represents the intensity of the EASM, a middle Holocene EASM maximum has been revealed (e.g., Chen et al., 2015a). Furthermore, contrasting spatial patterns of precipitation variability in eastern monsoonal China have been observed on various timescales (e.g., Ding et al., 2008; Chen et al., 2016; Liu et al., 2020a). For example, a dry middle Holocene with drought conditions in southern China contrasts with the middle Holocene precipitation maximum in northern China (Liu et al., 2020a). In addition, during the last millennium there was a north–south dipolar mode of precipitation in eastern China, which demonstrates that during the Medieval Climate Anomaly (MCA, 1000–1300 CE) the northern part of eastern China was generally wetter, while the southern part was generally drier compared with the Little Ice Age (LIA, 1400–1900 CE) (Chen et al., 2015b). This meridional difference in precipitation in eastern China was caused by the northward or southward movement of the western Pacific subtropical high (WPSH), which led to the pattern of ‘drought conditions in northern China and flooding in southern China’, and vice versa, in monsoonal eastern China (Ding et al., 2008; Zhou et al., 2009; Qian et al., 2011).

Besides its north–south movement, the WPSH also exhibits a pattern of west–east movement (Zhou et al., 2009), which has the possibility of causing an asynchronous east–west pattern of rainfall in central China. Although this asynchrony has not been documented on longer timescales, a systemic investigation of climatic records on a large spatial scale and on different timescales during the Holocene indicated that the climate in monsoonal northern and northeastern China shows an out-of-phase or anti-phased relationship with that in northwestern China and central Asia (Chen et al., 2019a). The boundary between wetter northern China and drier arid central Asia corresponded roughly to the modern summer monsoon boundary across the CLP (Chen et al., 2015b).

The western CLP, which is close to the modern summer monsoon boundary, is sensitive to variations in EASM precipitation. Due to their high sediment accumulation rate and high sensitivity to regional and global climate change, the loess deposits in the region have been investigated in order to reconstruct monsoon variability (e.g., Chen et al., 1997; Sun et al., 2012; Zhang et al., 2016). The overall consistency of the stratigraphy of the loess–paleosol sequences in the western and eastern CLP confirms the synchronicity of changes on the orbital timescale (Zhang et al., 2016). However, additional sub-paleosols layers and loess–interbedded units have been found in the core region in the western CLP (Zhang et al., 2016), potentially indicating that a different pattern of moisture variability may have existed in the western CLP on sub-orbital timescales compared with the eastern CLP. With regard to the Holocene, high-resolution loess records of monsoon precipitation from the western CLP are still lacking, especially those with a reliable chronology. Here we present climatic reconstructions from loess deposits with the age control based on two independent dating methods. Analyses of sedimentary facies, environmental magnetic indexes, organic carbon isotopes, and grain size are used to reconstruct the precipitation and atmospheric circulation variations since 15 ka. In addition, we compare the climatic records from the eastern and western CLP and use the results of a climate model simulation to evaluate the geological data. Our overall aim was to determine and interpret the spatial pattern of moisture evolution in the CLP during the present interglacial.

2. Geological setting

The CLP in central China is divided into three geographical regions by the Liupan and Lvliang Mountains (Liu, 1985). Here, we refer to the region to the west of the Liupan Mountains as the western CLP, and the eastern part as the eastern CLP. The present study area is the Ganjia

Basin in Xiahe county, Gansu Province, which is in the northeastern Tibetan Plateau and adjacent to the western CLP (Fig. 1). Loess deposits in the Ganjia Basin are widely distributed on pediments and river terraces, and are especially well-developed in the southwestern part of the basin and on the southern slopes of the Dalijia Mountains. Five loess sections have been investigated in the basin, and in this study we focus on two loess sections BSY19A (35°26′24.80″N, 102°34′2.14″E; 3191 m a.s.l.) and BSY20A (35°26′25.86″N, 102°34′1.16″E; 3192 m a.s.l.), which are located on the southern slopes of the Dalijia Mountains (Fig. S1). The two sections are on the eastern side of the Jiangla River, a small tributary of the Yangqu River in the Ganjia Basin, and ~1 km south of Baishiya karst cave (Fig. S1), which is an archaic *Homo* site where a late Middle Pleistocene Denisovan mandible dated to at least 160 ka was found (Chen et al., 2019b).

The climate of the CLP is controlled by the warm and humid southeasterly EASM during the warm season and by the cold and dry northwesterly East Asian winter monsoon (EAWM) during the cold season. Precipitation values at the nearest meteorological stations of Linxia (1,917 m a.s.l., 50 km east of the section), Xiahe (2,929 m a.s.l., 40 km south of the section) and Xunhua (1,921 m a.s.l., 40 km north of the section) (<http://cdc.cma.gov.cn>) were 501 mm, 448 mm, and 272 mm, respectively, during 1981–2010. The mean annual temperatures at the three stations during the same period were 7.3 °C, 3.4 °C and 8.9 °C, respectively. More than 80% of the annual total precipitation occurred between May and September, under the influence of the EASM (Fig. S2). Winter precipitation is minor and the climate under the prevailing northerly and northwesterly winds is mainly controlled by the location of the Siberian High. The landscape in the basin is steppe and the vegetation of the lower mountain slopes is typical grassland.

3. Materials and methods

3.1. Loess–paleosol sequences and sampling

Among the five loess–paleosol sections investigated in the Ganjia Basin (Table S1), the BSY19A section is 1.4-m thick (Figs. 2,3). The uppermost 75 cm of the section is an indurated paleosol with abundant plant roots in the top ~10 cm. Paleosol layers are dark brown clayey silt with abundant bio-pores and a crumb structure. From 75 cm to 140 cm a yellowish to light brown loess is present with no evidence of major pedogenesis or color changes. The loess layers are silt, with a compact structure. The boundaries between the weakly-altered loess and paleosol are readily discernable in the field. The topmost ~80-cm dark Holocene paleosol layer, underlain by loess is widely distributed along the slopes in the area and thus the sedimentary facies and magnetic susceptibility stratigraphy of the five sections show a very consistent pattern of variations (Fig. S3). Bulk samples were collected at 1-cm intervals in each section, with 140 samples obtained from the BSY19A section.

3.2. Dating and climate indexes

Twelve bulk organic samples were collected with a relatively equal interval from the BSY19A section for accelerator mass spectrometry (AMS) ¹⁴C dating, which was conducted by Beta Analytic, USA. Samples were pretreated with acid washing, and standard analytical methods were used (Olsson, 1986). Calibration to calendar ages was undertaken using IntCal20 (Northern Hemisphere; Reimer et al., 2020). The carbon isotope ratio ($\delta^{13}\text{C}$) of the bulk organic matter was also measured by Beta Analytic. The reliability of the chronology of the loess–paleosol deposits in the Ganjia Basin was confirmed by optically stimulated luminescence (OSL) dating of five samples from section BSY20A, which is adjacent to section BSY19A. Sample preparation for OSL dating followed the procedures of Aitken (1998). OSL measurements of coarse-grained (63–90 μm) quartz were conducted using an automated Risø TL/OSL-DA-20 reader at the MOE Key Laboratory of Western China's Environmental Systems, Lanzhou University. A single aliquot

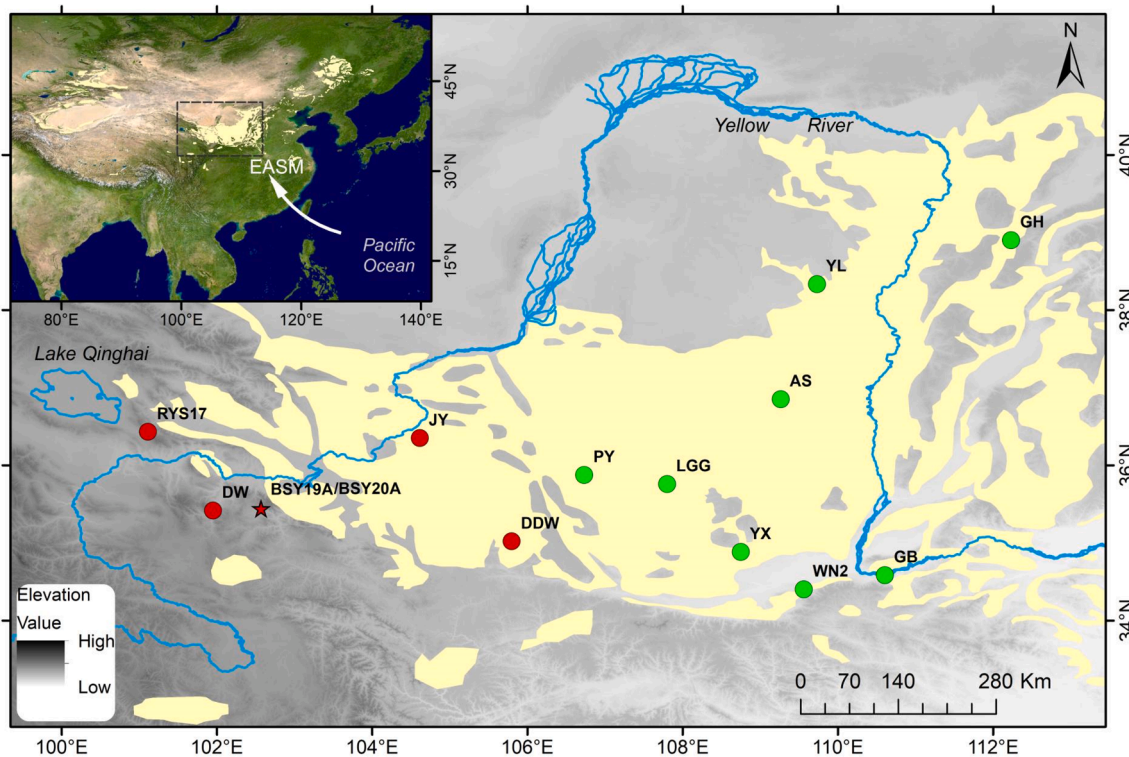


Fig. 1. Map of the Chinese Loess Plateau showing the locations of the studied sections and the cited records. See Table S2 for the site abbreviations. Inset map shows the location of the Chinese Loess Plateau.

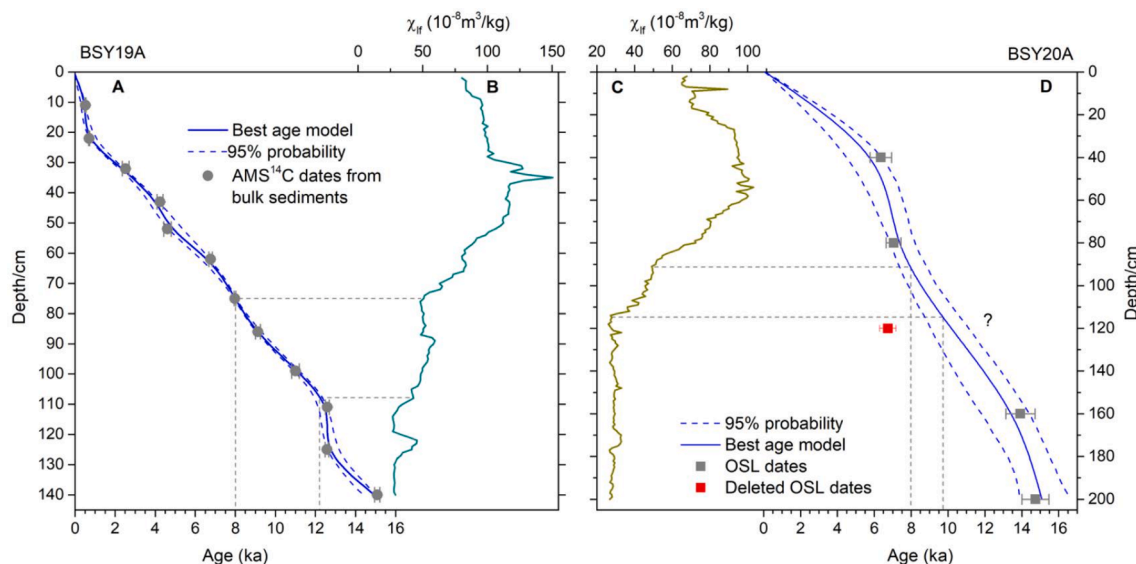


Fig. 2. Age-depth models for loess sections BSY19A (B) and BSY20A (D) in the western Chinese Loess Plateau and their magnetic susceptibility records (B and C).

regenerative (SAR) protocol (Murray and Wintle, 2003) was used to measure the De (equivalent dose) of the quartz samples.

After air-drying in the laboratory, 140 weighed samples were packed into $2 \times 2 \times 2 \text{ cm}^3$ plastic boxes and measured for low-frequency (470 Hz) and high-frequency (4,700 Hz) magnetic susceptibility (MS) (χ_{lf} and χ_{hf} , respectively) using a Bartington Instruments MS2B magnetic susceptibility meter. The frequency-dependence of magnetic susceptibility (χ_{fd}), which reflects the content of fine-grained ferrimagnetic minerals of pedogenic origin, was calculated as χ_{lf}/χ_{hf} . The grain-size distributions of all of the samples from the section BSY19A were measured using a Malvern Mastersizer 2000 laser grain size analyzer. Grain size frequency

distributions were calculated for 100 grain-size classes within a measuring range of 0.02–2000 μm , with an analytical error of less than 1%. The samples were pretreated with 10% H_2O_2 to remove organic matter and then with 10 ml of 10% HCl to remove carbonates. About 100 ml deionized water was then added and the samples were kept stationary for 12 h. After the supernatant was siphoned off, 10 ml of 0.05 mol/L $(\text{NaPO}_3)_6$ were added as a dispersant and the samples were then ultrasonicated for 5 min prior to grain-size measurements. The measurements of grain size and MS were conducted in the MOE Key Laboratory of Western China’s Environmental Systems, Lanzhou University.

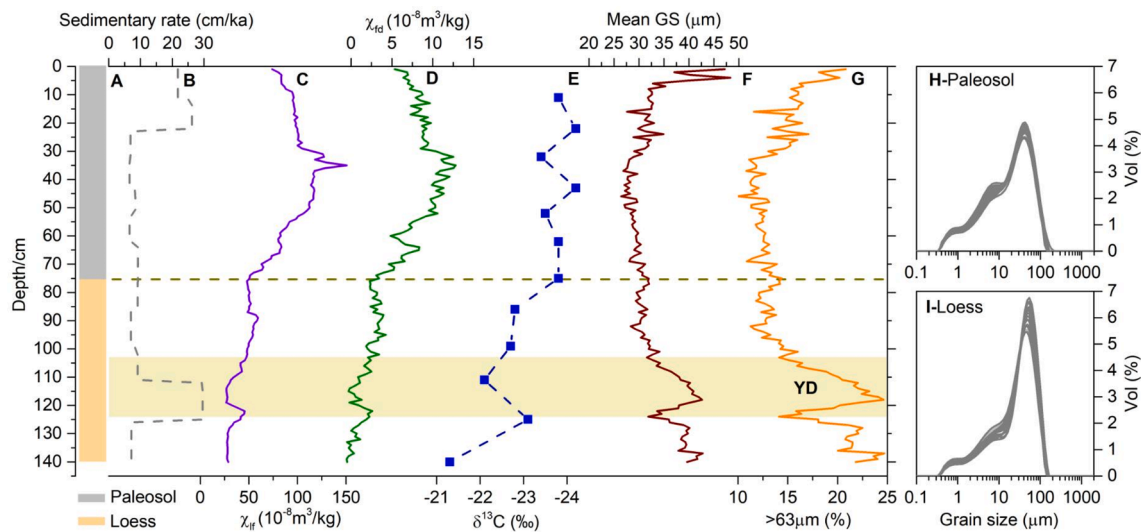


Fig. 3. Lithology, age-depth model, and proxies for the section BSY19A on the western Chinese Loess Plateau.

3.3. Climate model simulation

In order to investigate the pattern of Holocene moisture variability in the CLP, we used 15 climate simulations for the middle Holocene (6 ka) and the pre-industrial period (PI, 1850 CE) from the Paleoclimate Modelling Intercomparison Project Phase III (PMIP3). The simulations were performed using eight atmosphere–ocean coupled general circulation models (AOGCMs) and seven atmosphere–ocean–vegetation general circulation models (AOVGCMs). Basic information about these models is provided in Table 1. The main boundary conditions for the middle Holocene experiment included the Earth's orbital configuration

Table 1
Basic information on the general circulation models used in the present study.

Numbers	Model ID	Project	Atmospheric resolution	Length of run analyzed (year)	Baseline period
1	BCC-CSM1.1	PMIP3 (AOVGCM)	T42L26	100	Pre-industrial
2	CCSM4	PMIP3 (AOGCM)	288 × 192, L26	301	Pre-industrial
3	CNRM-CM5	PMIP3 (AOGCM)	256 × 128, L31	200	Pre-industrial
4	CSIRO-Mk3-6-0	PMIP3 (AOGCM)	192 × 96, L18	100	Pre-industrial
5	CSIRO-Mk3L-1-2	PMIP3 (AOGCM)	64 × 56, L18	500	Pre-industrial
6	EC-EARTH-2-2	PMIP3 (AOGCM)	320 × 160, L62	40	Pre-industrial
7	FGOALS-g2	PMIP3 (AOVGCM)	128 × 60, L26	100	Pre-industrial
8	FGOALS-s2	PMIP3 (AOVGCM)	128 × 108, L26	100	Pre-industrial
9	GISS-E2-R	PMIP3 (AOGCM)	144 × 90, L40	100	Pre-industrial
10	HadGEM2-CC	PMIP3 (AOVGCM)	192 × 145, L60	35	Pre-industrial
11	HadGEM2-ES	PMIP3 (AOVGCM)	192 × 145, L38	102	Pre-industrial
12	IAP-FGOALS-G2.3	PMIP3 (AOVGCM)	96 × 95, L39	500	Pre-industrial
13	MIROC-ESM	PMIP3 (AOVGCM)	T42L80	100	Pre-industrial
14	MPI-ESM-P	PMIP3 (AOGCM)	T63L47	100	Pre-industrial
15	MRI-CGCM3	PMIP3 (AOGCM)	320 × 160, L48	100	Pre-industrial

and atmospheric greenhouse gas concentrations (Taylor et al., 2012; Tian and Jiang, 2015). In the middle Holocene simulation, the orbital parameters were fixed at 6 ka, with an eccentricity of 0.018682, an obliquity of 24.105°, and a longitude of the perihelion of 0.87°, which were significantly different from those of the PI (Berger and Loutre, 1991). The atmospheric concentrations of CO₂, CH₄, and N₂O during the middle Holocene were 280 ppm, 650 ppb, and 270 ppb, respectively, which were different to the values of 284 ppm, 791 ppb, and 275 ppb during the PI. Other boundary conditions, including aerosols, solar constant, ice sheets, topography, and coastlines during the middle Holocene were the same as in the PI experiments. The vegetation of the middle Holocene simulations was the same as in the PI experiments while using the AOGCMs. In the AOVGCMs simulations the vegetation is interactive for both the middle Holocene and the PI. Further details of the boundary conditions for the middle Holocene and the PI can be found at <http://pmip3.lscce.ipsl.fr>.

4. Results and discussion

4.1. Chronology of loess deposits in the Ganjia Basin

The AMS ¹⁴C dating results for section BSY19A are listed in Table 2. All of the radiocarbon ages were calibrated to calendar years using CALIB 8.0.1. A final age-depth model (Fig. 2A) was established using a smoothing spline approach with the Clam package in R updated with the IntCal20 calibration curve (Blaauw, 2010; Reimer et al., 2020). The resulting chronology yielded an average temporal resolution of ~107 yr for the grain size and MS measurements, and the mean sediment accumulation rate is ~10 cm/kyr for the whole section. Compared with the majority of Holocene sections previously investigated in the western CLP, the section has a relatively low sediment accumulation rate (Fig. 3B).

To confirm the reliability of the chronology of loess-paleosol deposits in the Ganjia Basin, we conducted OSL dating of a parallel section and the dating results for five samples are listed in Table 3. The age of the depth of 120 cm was excluded from the age model because it is much younger than would be expected on the basis of the date above it. The sample may possibly include younger material introduced via a rodent burrow (Fig. S4), (despite our attempts to avoid them during field sampling), resulting in the age underestimation. The final age-depth model was established based on four dates and using the same approach used for the radiocarbon dates. The chronological framework of section BSY20A indicates that the paleosol with high MS values developed after 8 ka, which is also the case for section BSY19A,

Table 2
AMS ^{14}C ages for the BSY19A loess section in the western Chinese Loess Plateau.

Beta No.	Sample No.	Depth/ cm	Materials	Conventional Radiocarbon Age (without $\delta^{13}\text{C}$ correction)	Measured Radiocarbon Age	Calendar age calibrated with IntCal20 (95% Probability)	IRMS $\delta^{13}\text{C}/\text{‰}$
Beta - 563,755	BSY19 10- 11	11	Organic sediment	500 \pm 30 BP	480 \pm 30 BP	541–497 cal BP	–23.8
Beta - 561,697	BSY19 21- 22	22	Organic sediment	790 \pm 30 BP	780 \pm 30 BP	728–672 cal BP	–24.2
Beta - 563,756	BSY19 31- 32	32	Organic sediment	2430 \pm 30 BP	2400 \pm 30 BP	2698–2354 cal BP	–23.4
Beta - 561,698	BSY19 42- 43	43	Organic sediment	3830 \pm 30 BP	3820 \pm 30 BP	4393–4093 cal BP	–24.2
Beta - 563,757	BSY19 51- 52	52	Organic sediment	4080 \pm 30 BP	4060 \pm 30 BP	4791–4423 cal BP	–23.5
Beta - 561,699	BSY19 61- 62	62	Organic sediment	5960 \pm 30 BP	5940 \pm 30 BP	6849–6671 cal BP	–23.8
Beta - 561,700	BSY19 74- 75	75	Organic sediment	7180 \pm 30 BP	7160 \pm 30 BP	8021–7934 cal BP	–23.8
Beta - 563,758	BSY19 85- 86	86	Organic sediment	8170 \pm 30 BP	8130 \pm 30 BP	9252–8997 cal BP	–22.8
Beta - 563,759	BSY19 98- 99	99	Organic sediment	9700 \pm 30 BP	9660 \pm 30 BP	11192–10808 cal BP	–22.7
Beta - 561,701	BSY19 110- 111	111	Organic sediment	10,630 \pm 30 BP	10,580 \pm 30 BP	12692–12491 cal BP	–22.1
Beta - 563,760	BSY19 124- 125	125	Organic sediment	10,560 \pm 30 BP	10,530 \pm 30 BP	12666–12480 cal BP	–23.1
Beta - 561,702	BSY19 139- 140	140	Organic sediment	12,710 \pm 40 BP	12,650 \pm 40 BP	15217–14951 cal BP	–21.3

Table 3
Data related to the quartz OSL age determination from the BSY20A section.

Lab. No.	Field No.	Depth (cm)	Grain size (μm)	U (ppm)	Th (ppm)	Rb (ppm)	K (%)	Water content (%)	Dose (Gy)	Dose Rate (Gy/ka)	Age (ka)
LZU20136	BSY20A- 40	40	63–90	2.25 \pm 0.3	12.68 \pm 0.70	97.88 \pm 5.00	1.85 \pm 0.04	10 \pm 5	19.16 \pm 1.62	3.02 \pm 0.12	6.352 \pm 0.589
LZU20139	BSY20A- 80	80	63–90	2.31 \pm 0.3	12.33 \pm 0.70	91.52 \pm 5.00	1.83 \pm 0.04	10 \pm 5	20.91 \pm 0.87	2.97 \pm 0.12	7.046 \pm 0.401
LZU20137	BSY20A- 120	120	63–90	2.37 \pm 0.3	12.85 \pm 0.70	97.67 \pm 5.00	1.84 \pm 0.04	10 \pm 5	21.18 \pm 1.08	3.14 \pm 0.13	6.737 \pm 0.438
LZU20135	BSY20A- 160	160	63–90	2.36 \pm 0.3	12.34 \pm 0.70	87.78 \pm 4.00	1.82 \pm 0.04	10 \pm 5	44.51 \pm 1.73	3.20 \pm 0.13	13.924 \pm 0.795
LZU20138	BSY20A- 200	200	63–90	2.49 \pm 0.3	13.23 \pm 0.70	87.70 \pm 4.00	1.83 \pm 0.04	10 \pm 5	50.26 \pm 1.22	3.41 \pm 0.15	14.734 \pm 0.732

suggesting that the chronology of these loess sections in the Ganjia Basin is robust.

4.2. Holocene moisture variations recorded by BSY19A section

The lithostratigraphy of loess deposits is usually characterized by well-developed loess and paleosol alternations, which reflect moisture variations: during intervals of relatively dry (humid) climate, eolian dust is deposited (or a paleosol is formed) (An et al., 1991; Porter, 2001). Thus, loess deposits are well suited for reconstructing moisture changes on Earth orbital timescales (Porter, 2001), and even on the millennial scale (Chen et al., 1997; Sun et al., 2012; Rao et al., 2013). The grain size of loess-paleosol sections in the CLP is commonly used as an index of the EAWM intensity on glacial-interglacial timescales (An et al., 1991), as well as during the Holocene (Kang et al., 2020). The grain-size data from the section BSY19A reveal a persistent weakening of the EAWM since the last deglaciation and an increase during the Younger Dryas (YD) event (Fig. 4a, b). A weakened EAWM occurred during 10–3 ka, followed by a subsequent intensification during the late Holocene. The changes in the EAWM during the Holocene revealed by climate proxy records from the CLP are broadly consistent (Xia et al., 2014; Kang et al., 2020), although a recent study proposed an early Holocene EAWM weakening and a middle-to-late Holocene strengthening (Kang et al., 2020).

With regard to soil development, the χ_{lf} values are low and uniform during ~15–13 ka, with a decreasing trend during the YD event

(Fig. 4d). The values are slightly higher during the early Holocene compared with the late Pleistocene. There is a pronounced increase in χ_{lf} from 8 ka onwards, with a maximum at ~3 ka, and a decrease thereafter. The content of fine-grained particles (Fig. 4c; $<4\mu\text{m}$) and the χ_{fd} values (Fig. 4e) show the same pattern of variation as χ_{lf} , but with a clearer pattern of fluctuations. The variation in MS is closely linked with pedogenesis during which fine-grained ferrimagnetic particles (e.g., magnetite and maghemite) are formed and which are commonly used as an indicator of summer monsoon (moisture or rainfall) intensity in the CLP (An et al., 1991; Chen et al., 1997; Balsam et al., 2011). The content of pedogenic magnetite and maghemite is strongly correlated with soil moisture and its seasonal variation (Maher, 2016). On this basis, the magnetic proxies indicate that the moisture level in the study region was low during the early Holocene and was enhanced after 8 ka.

The value of $\delta^{13}\text{C}$ of the bulk organic matter varies from –24.2 ‰ to –21.3 ‰, with a pronounced increase during the YD event and more negative values after 8 ka (Fig. 4f). Although a study of loess records from the CLP indicated that an increase in the relative abundance of C_4 plants from the last glacial to the Holocene (Yang et al., 2015), the range of $\delta^{13}\text{C}$ values in section BSY19A in the Ganjia Basin indicates that the local terrestrial ecosystem was dominated by, or composed entirely of, C_3 plants. Various studies have shown that the $\delta^{13}\text{C}$ of modern C_3 plants responds principally to precipitation variations, with increasing precipitation resulting in more negative $\delta^{13}\text{C}$ values (Wang et al., 2003; Rao et al., 2013). Thus the $\delta^{13}\text{C}$ record, although of relatively low

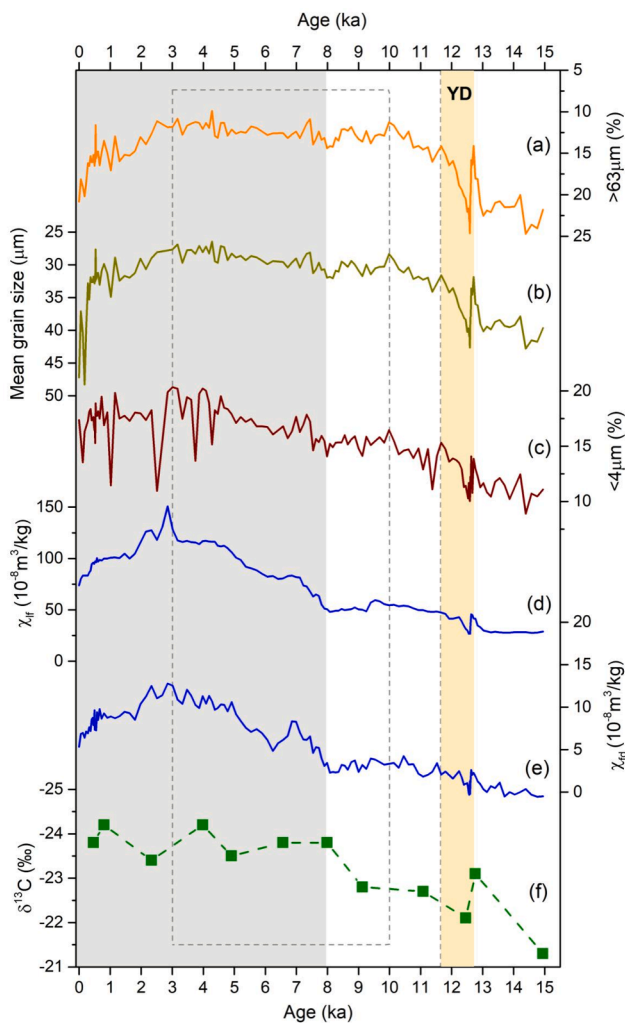


Fig. 4. Time series of climatic indexes for section BSY19A.

stratigraphic resolution, reveals an increase in precipitation after 8 ka in the Ganjia Basin. In summary, the dark Holocene paleosols with high MS values and negative $\delta^{13}\text{C}$ values since 8 ka represent increased moisture, or possibly precipitation, during the middle to late Holocene.

4.3. Differences in the pattern of Holocene moisture evolution in the western and eastern CLP

Our humidity reconstructions are in agreement with loess-based precipitation records from the western CLP (Table S2). As shown in Fig. 5b–e, the magnetic indexes and MS-based paleoprecipitation reconstruction from the loess sections at Dadiwan (DDW; Liu et al., 2020b), Riyueshan (RYS; Li et al., 2020), Duowa (DW; Maher and Hu, 2006), and Jingyuan (JY; Sun et al., 2010) in the western CLP show much higher values during the middle to late Holocene compared with the early Holocene. There is also a decreasing trend or lower values of the magnetic indexes after 3 ka. Among the cited precipitation reconstructions from the western CLP, that of the DW section demonstrates a major peak at the beginning of the Holocene and an overall increasing trend during the middle to late Holocene (Maher and Hu, 2006). For the adjacent region beyond the western CLP, the water level of Lake Qinghai is suggested to have been low during the early Holocene, followed by an increase after ~8 ka when a relatively high lake level was maintained (Wang et al., 2019 and references therein). A similar situation was also found in the case of Lake Dalianhai in the Gonghe Basin, south of Lake Qinghai (Wu et al., 2020). Combining all of

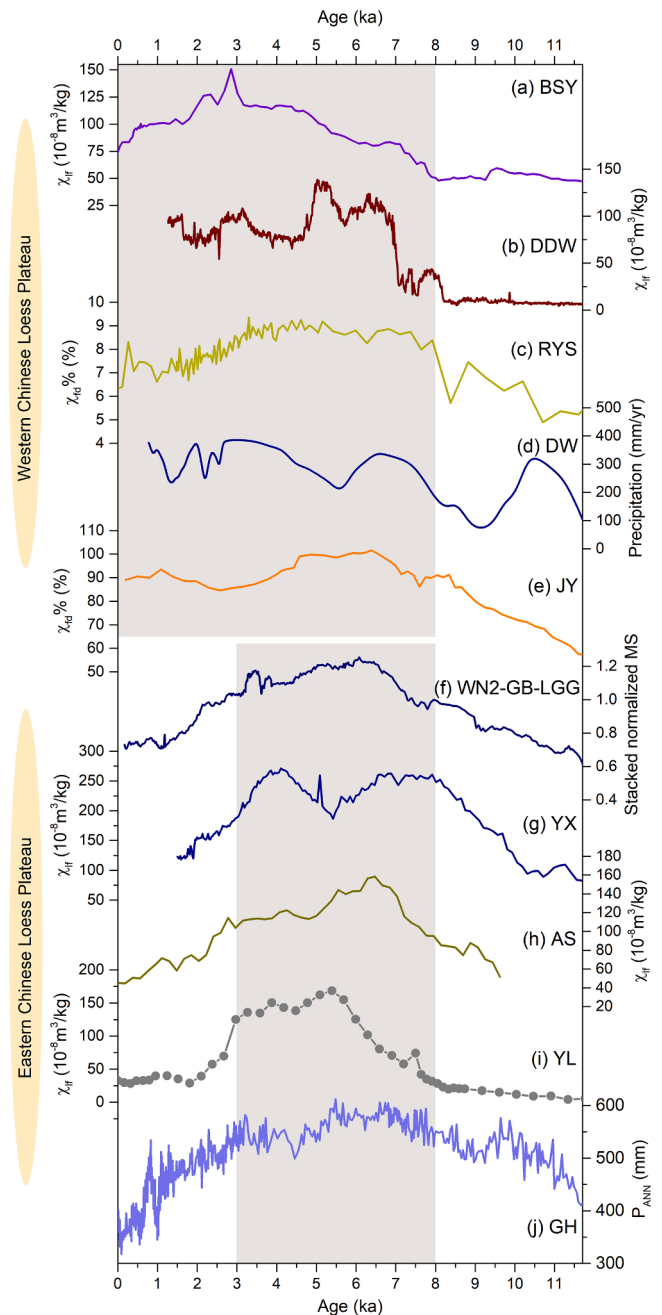


Fig. 5. Comparison of moisture indexes from the western and eastern Chinese Loess Plateau. The locations and details of the records can be found in Fig. 1 and Table S2.

this evidence, we conclude that a relatively wet climatic phase occurred during the middle to late Holocene in the western CLP, as well as in the adjacent regions to the west.

In the eastern CLP, the region east of the Liupan Mountains, the moisture or precipitation variations during the Holocene are well documented in several loess-paleosol sections (Table S2). Studies of the loess sections at Yulin (YL; Lu et al., 2013), Yaoxian (YX, Xia et al., 2014), Ansai (AS; Gao et al., 2019) and Pengyang (PY; Gao et al., 2019) show that the MS reached its highest values during 8–3 ka, with lower values during both the early and late Holocene. This finding is supported by results from other loess sections: e.g., Weinan (WN; Kang et al., 2020), Gaobei (GB; Kang et al., 2020), and Longgugou (LGG; Kang et al., 2020) in the eastern CLP. Soil development occurred at many locations across the CLP during the middle Holocene. However, this optimum

climate was then interrupted by the development of an arid climate in the eastern CLP, which is indicated by the deposition of the relatively coarse-grained loess unit (L0) (e.g., Kang et al., 2020). In addition, a pollen-based precipitation record from the sediments of Lake Gonghai in the eastern CLP reveals a gradually intensifying monsoon during the early Holocene, with maximum monsoon intensity during ~7.8–5.3 ka, and a rapidly weakening monsoon after ~3.3 ka (Chen et al., 2015a; Fig. 5j).

As soil development is closely linked with moisture conditions, the records from loess-paleosol sequences usually reflect moisture variations. Although high precipitation typically results in enhanced moisture conditions, evaporation is also an important control. Evaporation intensity is dominated by temperature and wind conditions. Considering the consistency of temperature variations on a large spatial scale and the similarity of wind conditions, including variations in the EAWM in the CLP during the Holocene (Kang et al., 2020), we suggest that moisture variations in the CLP were controlled by changes in precipitation amount. Therefore, based on our reconstruction and the foregoing comparison with other records from the CLP, we conclude that there was an east–west asymmetry in precipitation in the CLP during the Holocene. Precipitation in the CLP was low during the early Holocene and increased during 8–3 ka; however, precipitation in the western CLP was much higher after 3 ka compared with the early Holocene, which is quite different from the Holocene evolution of precipitation in the eastern CLP.

The simulation results also suggest the occurrence of wetter conditions (compared to the PI) in the eastern CLP during the middle Holocene, and the opposite in the western CLP. In detail, as shown in Fig. 6, the results of changes in summer precipitation between the middle Holocene (6 ka) and the PI (0 ka) from the ensemble mean of the PMIP3 simulations indicate that summer precipitation in the western CLP during the middle Holocene was slightly lower than today; however, an opposite pattern occurred in the eastern CLP, with enhanced precipitation during the middle Holocene compared with the most recent pre-industrial period. Therefore, the simulation results are in good agreement with the geological evidence.

4.4. Possible forcing mechanism of the westward migration of the rain belt in the CLP during the Holocene

It is widely accepted that the EASM is the principal control of the precipitation variability in the CLP. A previous study has highlighted the complexity of EASM dynamics since the last deglaciation. With the increase in Northern Hemisphere summer insolation since the last deglaciation (Berger and Loutre, 1991), the intensity of the EASM increased as

a result of the strengthened land-sea thermal contrast, which resulted in enhanced precipitation in the CLP (Chen et al., 2015a). As a possible consequence of the melting remnant Laurentide ice sheet, which continuously delivered freshwater to the North Atlantic until ~7–8 ka (Dyke, 2004; Fig. 7d), the EASM was weakened, leading to its lagged response to maximum in summer insolation (Chen et al., 2015a; Fig. 7e). Numerous climate simulation results have demonstrated that an anomalous freshening of the North Atlantic and the resulting weakened Atlantic Meridional Overturning Circulation (AMOC) could strongly depress the insolation-driven EASM (e.g., Chen et al., 2015a). Following the insolation decrease during the late Holocene (Fig. 7e), there was a significant decrease in the intensity of the EASM (hence precipitation) in the eastern CLP (Fig. 7b).

The WPSH is one of the most important components of the EASM system (Rodwell and Hoskins 2001). The intensity, structure, and location of the WPSH are characterized by a seasonal cycle, interannual changes, and long-term variations (Zhou et al., 2009). Thus variations in the WPSH on multiple timescales can cause flooding, drought, and heat waves in East Asia (Zhou et al., 2009; Dong and He, 2020). The seasonal variation of the WPSH is closely related to the onset and withdrawal of the EASM. In July, with the intensification of the WPSH and the extension of its boundary towards the Asian continent, precipitation increases zonally from East China to Japan. As the WPSH boundary approaches the continent during August, precipitation approaches the continent significantly over coastal areas but increases in northern China (Choi and Kim, 2019), and finally, in September, the WPSH boundary penetrates the continent. In addition, the two intervals of pronounced westerly extension (early–middle September and middle–late October)

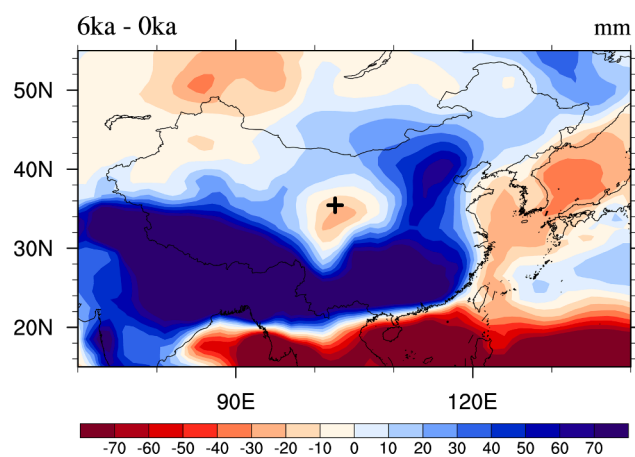


Fig. 6. Changes in summer precipitation (mm) between the middle Holocene (6 ka) and the preindustrial period (0 ka) from the ensemble mean of the 15 PMIP3 simulations (Table 1).

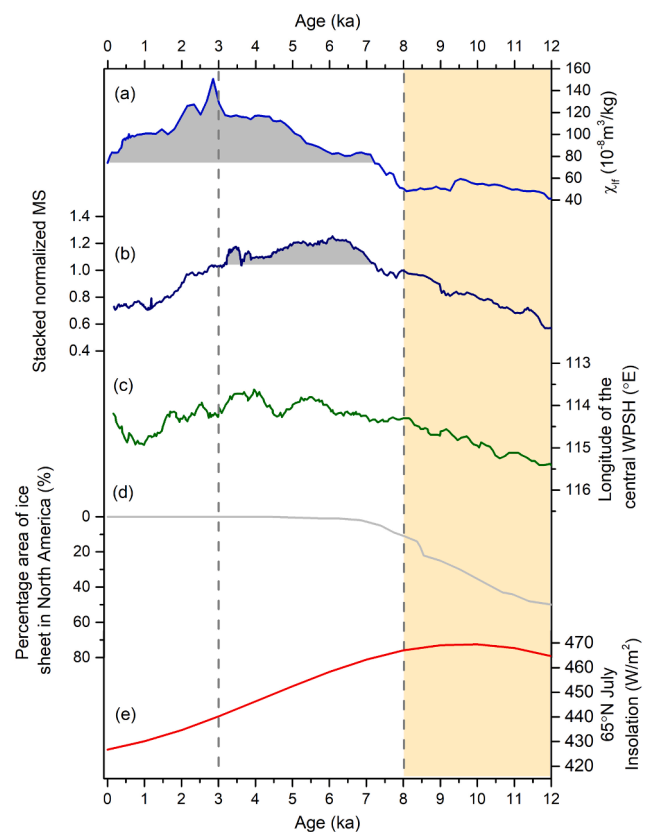


Fig. 7. Dynamics of precipitation variations in the Chinese Loess Plateau during the Holocene. (a) MS record of the BSY19A loess section from the western Chinese Loess Plateau; (b) stacked normalized MS record from loess sections in the eastern Chinese Loess Plateau (Kang et al., 2020); (c) longitude of the central western Pacific subtropical high based on the TraCE-21 ka simulation (Liu et al., 2014); (d) percentage area of ice sheets in North America (Dyke, 2004); (e) July solar insolation at 65°N (Berger and Loutre, 1991).

occur when the WPSH retreats southward, leading to the autumn rainy season in the southeastern parts of northwestern and western China (Yu, 2011).

In addition to the seasonal cycle, the WPSH also exhibits interannual changes. Since late 1970s, the WPSH has extended westwards, resulting in a shift of the rain belt over China, with excessive rainfall occurring along the middle and lower reaches of the Yangtze River valley, and a rainfall deficit in northern China (Yu and Zhou, 2007; Zhou et al., 2009). On a large spatial scale, increasing summer precipitation in arid central Asia has been suggested to be linked to the weakening of the EASM in recent decades, accompanied by a persistent westward shift of the WPSH and the increasing frequency of Mongolian anticyclone activity (Chen et al., 2020). It is suggested that the WPSH increase in extent and intensity, and its position extends westward (Liu et al., 2019). The low-level jet along the northwestern edge of the WPSH transports large amounts of water vapor into East Asia; hence any change in the WPSH would influence the monsoonal front by affecting the convergence of tropical water vapor with extratropical airflow (Ninomiya and Kobayashi, 1999; Zhou et al., 2009).

On a longer timescale, the location of the WPSH potentially has a significant influence on rainfall in the CLP. Based on a TraCE-21 ka simulation (Liu et al., 2014; Xu et al., 2020), the longitude of the central WPSH was reconstructed; as shown in Fig. 7c, the WPSH shows a westward movement during the early to middle Holocene and an overall eastward shift after 3 ka, with a relatively western location during 8–3 ka. Such a WPSH configuration would result in increased precipitation in the western CLP.

5. Conclusions

We have investigated five loess-paleosol sequences in the Ganjia Basin in Xiahe county, Gansu Province, China. The loess sections are composed of an indurated paleosol layer in the uppermost ~60–80 cm and an underlying loess deposit. The analysis of various climate proxies is used to construct a 15,000-year moisture/rainfall record with robust age control for the western CLP. Combining the results of measurements of magnetic susceptibility, grain size, and organic carbon isotopes from the 140-cm-long BSY19A section, we infer that precipitation was low during ~15–8 ka and increased after 8 ka, with a precipitation maximum occurring during 8–3 ka. A comparison with loess deposits and lacustrine records from the entire CLP indicates a pattern of east–west asymmetry in precipitation in the region during the Holocene. Precipitation in the CLP was low during the early Holocene, under the influence of a weak EASM, while a middle Holocene EASM maximum resulted in a high precipitation in the CLP during 8–3 ka. However, precipitation in the western CLP after 3 ka was much higher than during the early Holocene, which was quite different to the situation in the eastern CLP. These conclusions are supported by the results of numerical modeling experiments. Finally, we propose that a westward extension of the WPSH was responsible for the observed spatial pattern of precipitation in the CLP during the Holocene.

Declaration of Competing Interest

The authors declare that they have no known competing financial interests or personal relationships that could have appeared to influence the work reported in this paper.

Acknowledgements

This work was supported by the Second Tibetan Plateau Scientific Expedition and Research Program (STEP) (award 2019QZKK0601), the National Natural Science Foundation of China (awards 41807442, 41991251), and the Fundamental Research Funds for the Central Universities (award lzujbky-2020-73). We thank Prof. Jiawu Zhang, Prof. Chengbang An, Dr. Benhong Guo, Dr. Yuan Li, and Dr. Qiang Wang for

constructive discussions; and thank Mr. Yuanlong Luo for help with the field work.

Appendix A. Supplementary material

Supplementary data to this article can be found online at <https://doi.org/10.1016/j.catena.2021.105626>.

References

- Aitken, M.J., 1998. *An Introduction to Optical Dating*. Oxford University Press, Oxford, UK.
- An, Z.S., Kukla, G.J., Porter, S.C., Xiao, J.L., 1991. Evidence of monsoon variation on the Loess Plateau of central China during the last 130,000 years. *Quat. Res.* 36, 29–36.
- An, Z.S., Porter, S.C., Kutzbach, J.E., Wu, X.H., Wang, S.M., Liu, X.D., Li, X.Q., Zhou, W. J., 2000. Asynchronous Holocene optimum of the East Asian monsoon. *Quat. Sci. Rev.* 19, 743–762.
- Balsam, W.L., Ellwood, B.B., Ji, J., Williams, E.R., Long, X., Hassani, A.E., 2011. Magnetic susceptibility as a proxy for rainfall: Worldwide data from tropical and temperate climate. *Quat. Sci. Rev.* 30, 2732–2744.
- Berger, A., Loutre, M.F., 1991. Insolation values for the climate of the last 10 million years. *Quat. Sci. Rev.* 10, 297–317.
- Blaauw, M., 2010. Methods and code for ‘classical’ age-modelling of radiocarbon sequences. *Quat. Geochronol.* 5, 512–518.
- Chen, C.Z., Zhang, X.J., Lu, H.Y., Jin, L.Y., Du, Y., Chen, F.H., 2020. Increasing summer precipitation in arid Central Asia linked to the weakening of the East Asian summer monsoon in the recent decades. *Int. J. Climatol.* 1–15.
- Chen, F.H., Bloemendal, J., Wang, J.M., Li, J.J., Oldfield, F., Ma, Y.Z., 1997. High-resolution multi-proxy climate records from Chinese loess: evidence for rapid climatic changes over the last 75 kyr. *Paleogeogr. Paleoclimatol. Paleoecol.* 130, 323–335.
- Chen, F.H., Chen, J.H., Huang, W., Chen, S.Q., Huang, X.Z., Jin, L.Y., Jia, J., Zhang, X.J., An, C.B., Zhang, J.W., Zhao, Y., Yu, Z.C., Zhang, R.H., Liu, J.B., Zhou, A.F., Feng, S., 2019a. Westerlies Asia and monsoonal Asia: Spatiotemporal differences in climate change and possible mechanisms on decadal to sub-orbital timescales. *Earth-Sci. Rev.* 192, 337–354.
- Chen, F.H., Welker, F., Shen, C.C., Bailey, S.E., Bergmann, I., Davis, S., Xia, H., Wang, H., Fischer, R., Freidline, S.E., Yu, T.L., Skinner, M.M., Stelzer, S., Dong, G.R., Fu, Q.M., Dong, G.H., Wang, J., Zhang, D.J., Hublin, J.J., 2019b. A late Middle Pleistocene Denisovan mandible from the Tibetan Plateau. *Nature* 569, 7756.
- Chen, F.H., Xu, Q.H., Chen, J.H., Birks, H.J.B., Liu, J.B., Zhang, S.R., Jin, L.Y., An, C.B., Telford, R.J., Cao, X.Y., Wang, Z.L., Zhang, X.J., Selvaraj, K., Lu, H.Y., Li, Y.C., Zheng, Z., Wang, H.P., Zhou, A.F., Dong, G.H., Zhang, J.W., Huang, X.Z., Bloemendal, J., Rao, Z.G., 2015a. East Asian summer monsoon precipitation variability since the last deglaciation. *Sci. Rep.* 5, 11186.
- Chen, J.H., Chen, F.H., Feng, S., Huang, W., Liu, J.B., Zhou, A.F., 2015b. Hydroclimatic changes in China and surroundings during the medieval climate Anomaly and Little Ice Age: spatial patterns and possible mechanisms. *Quat. Sci. Rev.* 107, 98–111.
- Chen, J.H., Rao, Z.G., Liu, J.B., Huang, W., Feng, S., Dong, G.H., Hu, Y., Xu, Q.H., Chen, F.H., 2016. On the timing of the East Asian summer monsoon maximum during the Holocene—Does the speleothem oxygen isotope record reflect monsoon rainfall variability? *Sci. China-Earth Sci.* 59, 2328–2338.
- Choi, W., Kim, K.Y., 2019. Summertime variability of the western North Pacific subtropical high and its synoptic influences on the East Asian weather. *Sci. Rep.* 9, 7865.
- Ding, Y., Wang, Z.Y., Sun, Y., 2008. Inter-decadal variation of the summer precipitation in East China and its association with decreasing Asian summer monsoon. Part I: Observed evidences. *Int. J. Climatol.* 28, 1139–1161.
- Dong, X., He, C., 2020. Zonal displacement of the Western North Pacific subtropical high from early to late summer. *Int. J. Climatol.* 40, 5029–5041.
- Dyke, A.S., 2004. An outline of North American Deglaciation with emphasis on central and northern Canada. *Devel. Quatern. Sci.* 2, 373–424.
- Gao, F.Y., Jia, J., Xia, D.S., Lu, C.C., Lu, H., Wang, Y.J., Liu, H., Ma, Y.P., Li, K.M., 2019. Asynchronous Holocene Climate Optimum across mid-latitude Asia. *Paleogeogr. Paleoclimatol. Paleoevol.* 518, 206–214.
- Kang, S.G., Du, J.H., Wang, N., Dong, J.B., Wang, D., Wang, X.L., Qiang, X.K., Song, Y.G., 2020. Early Holocene weakening and mid- to late Holocene strengthening of the East Asian winter monsoon. *Geology* 48, 1043–1047.
- Li, G.Q., Zhang, H.X., Liu, X.L., Yang, H., Wang, X.Y., Zhang, X.J., Jonell, T.N., Zhang, Y. N., Huang, X., Wang, Z., Wang, Y.X., Yu, L.P., Xia, D.S., 2020. Paleoclimatic changes and modulation of East Asian summer monsoon by high-latitude forcing over the last 130,000 years as revealed by independently dated loess-paleosol sequences on the NE Tibetan Plateau. *Quat. Sci. Rev.* 237, 106283.
- Liu, J.B., Shen, Z.W., Chen, W., Chen, J., Zhang, X., Chen, J.H., Chen, F.H., 2020a. Dipolar mode of precipitation changes between north China and the Yangtze River Valley existed over the entire Holocene: Evidence from the sediment record of Nanyi Lake. *Int. J. Climatol.* 1–15.
- Liu, T., 1985. *Loess and Environments*. China Ocean Press, Beijing.
- Liu, X.X., Sun, Y.B., Vandenberghe, J., Cheng, P., Zhang, X., Gowan, E.J., Lohmann, G., An, Z.S., 2020b. Centennial- to millennial-scale monsoon changes since the last deglaciation linked to solar activities and North Atlantic cooling. *Clim. Past.* 16, 315–324.

- Liu, Y.Y., Liang, P., Sun, Y., 2019. Simulations and Projections of the Western Pacific Subtropical High. In: *The Asian Summer Monsoon Characteristics. Teleconnections and Projection*. Elsevier Inc., Variability, pp. 179–198.
- Liu, Z., Lu, Z., Wen, X., Otto-Bliessner, B.L., Timmermann, A., Cobb, K.M., 2014. Evolution and forcing mechanisms of El Niño over the past 21,000 years. *Nature* 515, 550–553.
- Lu, H.Y., Yi, S.W., Liu, Z.Y., Mason, J.A., Jiang, D.B., Cheng, J., Stevens, T., Xu, Z.W., Zhang, E.L., Jin, L.Y., Zhang, Z.H., Guo, Z.T., Wang, Y., Otto-Bliessner, B., 2013. Variation of East Asian monsoon precipitation during the past 21 ky and potential CO₂ forcing. *Geology* 41, 1023–1026.
- Maher, B.A., 2016. Palaeoclimatic records of the loess/palaeosol sequences of the Chinese Loess Plateau. *Quat. Sci. Rev.* 154, 23–84.
- Maher, B.A., Hu, M., 2006. A high-resolution record of Holocene rainfall variations from the western Chinese Loess Plateau: antiphase behaviour of the African/Indian and East Asian summer monsoons. *The Holocene* 16, 68–76.
- Murray, A.S., Wintle, A.G., 2003. The single aliquot regenerative dose protocol: potential for improvements in reliability. *Radiat. Meas.* 37, 377–381.
- Ninomiya, K., Kobayashi, C., 1999. Precipitation and moisture balance of the Asian summer monsoon in 1991. Part II: Moisture transport and moisture balance. *J. Meteor. Soc. Japan* 77, 77–99.
- Olsson, I., 1986. Radiometric methods. In: Berglund, B. (Ed.), *Handbook of Holocene Palaeoecology and Palaeohydrology*. John Wiley and Sons, Chichester, pp. 273–312.
- Porter, S.C., 2001. Chinese loess record of monsoon climate during the last glacial-interglacial cycle. *Earth-Sci. Rev.* 54, 115–128.
- Qian, W.H., Zhu, Y.F., Tang, S.Q., 2011. Reconstructed index of summer monsoon dry-wet modes in East Asia for the last millennium. *Chin. Sci. Bull.* 56, 3019–3027.
- Rao, Z., Chen, F., Cheng, H., Liu, W., Wang, G., Lai, Z., Bloemendal, J., 2013. High-resolution summer precipitation variations in the western Chinese Loess Plateau during the last glacial. *Sci. Rep.* 3 (2786), 1–5.
- Reimer, P.J., Austin, W.E.N., Bard, E., Bayliss, A., Blackwell, P.G., Ramsey, C.B., Butzin, M., Cheng, H., Edwards, R.L., Friedrich, M., Grootes, P.M., Guilderson, T.P., Hajdas, I., Heaton, T.J., Hogg, A.G., Hughen, K.A., Kromer, B., Manning, S.W., Muscheler, R., Palmer, J.G., Pearson, C., Plicht, J., Reimer, R.W., Richards, D.A., Scott, E.M., Southon, J.R., Turney, C.S.M., Wacker, L., Adolphi, F., Büntgen, U., Capano, M., Fahrni, S., Fogtmann-Schulz, A., Friedrich, R., Köhler, P., Kudsk, S., Miyake, F., Olsen, J., Reinig, F., Sakamoto, M., Sookdeo, A., Talamo, S., 2020. The IntCal20 Northern Hemisphere radiocarbon age calibration curve (0–55 kcal BP). *Radiocarbon* 00, 1–33.
- Rodwell, M.J., Hoskins, B.J., 2001. Subtropical anticyclones and summer monsoon. *J. Climate* 14, 3192–3211.
- Shi, Y.F., Kong, Z.C., Wang, S.M., Tang, L.Y., Wang, F.B., Yao, T.D., Zhao, X.T., Zhang, P. Y., Shi, S.H., 1994. Climates and environments of the Holocene Megathermal Maximum in China. *Sci. China Ser. B* 37, 481–493.
- Sun, Y., Clemens, S.C., Morrill, C., Lin, X., Wang, X., An, Z., 2012. Influence of Atlantic meridional overturning circulation on the East Asian winter monsoon. *Nat. Geosci.* 5, 46–49.
- Sun, Y., Wang, X., Liu, Q., Clemens, S.C., 2010. Impacts of post-depositional processes on rapid monsoon signals recorded by the last glacial loess deposits of northern China. *Earth Planet. Sci. Lett.* 289, 171–179.
- Taylor, K.E., Stouffer, R.J., Meehl, G.A., 2012. An overview of CMIP5 and the experiment design. *Bull. Amer. Meteor. Soc.* 93, 485–498.
- Tian, Z.P., Jiang, D.B., 2015. Revisiting mid-Holocene temperature over China using PMIP3 simulations. *Atmos. Ocean. Sci. Lett.* 8, 358–364.
- Wang, G.A., Han, J.M., Liu, T.S., 2003. The carbon isotope composition of C3 herbaceous plants in loess area of northern China. *Sci. China Ser. D-Earth Sci.* 46, 1069–1076.
- Wang, H., He, Y., Liu, W., Zhou, A., Kolpakova, M., Krivonogov, S., Liu, Z., 2019. Lake water depth controlling archaeal tetraether distributions in midlatitude Asia: Implications for paleo lake - level reconstruction. *Geophys. Res. Lett.* 46, 5274–5283.
- Wang, H.P., Chen, J.H., Zhang, X.J., Chen, F.H., 2014. Palaeosol development in the Chinese Loess Plateau as an indicator of the strength of the East Asian summer monsoon: evidence for a mid-Holocene maximum. *Quat. Int.* 334–335, 155–164.
- Wu, D., Zhou, A.F., Zhang, J.W., Chen, J.H., Li, G.Q., Wang, Q., Chen L. Madsen, D., Abbott, M., Cheng, B., Chen F.H., 2020. Temperature-induced dry climate in basins in the northeastern Tibetan Plateau during the early to middle Holocene. *Quat. Sci. Rev.* 237, 106311.
- Xia, D., Jia, J., Li, G., Zhao, S., Wei, H., Chen, F., 2014. Out-of-phase evolution between summer and winter east Asian monsoons during the Holocene as recorded by Chinese loess deposits. *Quat. Res.* 81, 500–507.
- Xu, H., Goldsmith, Y., Lan, J.H., Tan, L.C., Wang, X.L., Zhou, X.Y., Cheng, J., Lang, Y.C., Liu, C.Q., 2020. Juxtaposition of western Pacific subtropical high on Asian summer monsoon shapes subtropical east Asian precipitation. *Geophys. Res. Lett.* 47 (3) e2019GL084705.
- Yang, S.L., Ding, Z.L., Li, Y.Y., Wang, X., Jiang, W.Y., Huang, X.F., 2015. Warming-induced northwestward migration of the East Asian monsoon rain belt from the Last Glacial Maximum to the mid-Holocene. *Proc. Natl. Acad. Sci. USA* 112 (43), 13178–13183.
- Yu, R., Zhou, T., 2007. Seasonality and three-dimensional structure of the interdecadal change in East Asian monsoon. *J. Climate* 20, 5344–5355.
- Yu, Y.X., 2011. Shift of the East Asian summer monsoon rain belt with the west Pacific subtropical high, the interdecadal variation of summer rainfall in China and several problems of Jiangsu climate change. PhD thesis. Lanzhou University.
- Zhang, J., Li, J.J., Guo, B.H., Ma, Z.H., Li, X.M., Ye, X.Y., Yu, H., Liu, J., Yang, C., Zhang, S.D., Song, C.H., Hui, Z.C., Peng, T.J., 2016. Magnetostratigraphic age and monsoonal evolution recorded by the thickest Quaternary loess deposit of the Lanzhou region, western Chinese Loess Plateau. *Quat. Sci. Rev.* 139, 17–29.
- Zhou, T., Yu, R., Zhang, J., Drange, H., Cassou, C., Deser, C., Hodson, D.L.R., Sanchez-Gomez, E., Li, J., Keenlyside, N., Xin, X.G., Okumura, Y., 2009. Why the Western Pacific subtropical high has extended westward since the late 1970s. *J. Clim.* 22, 2199–2215.